Robust Electromagnetic Control of Microrobots Under Force and Localization Uncertainties

Hamal Marino, Christos Bergeles, *Member, IEEE*, and Bradley J. Nelson, *Fellow, IEEE*

***Abstract*—Microrobots are promising tools for micromanipulation and minimally invasive interventions. Robust electromagnetic control of microrobots can be achieved through precisely modeled magnetic steering systems and accurate localization. Error-free modeling and position information, however, are not realistic assumptions, and microrobots need to be controlled under force and localization uncertainties. In this paper, methods to account for these types of uncertainties are presented. Initially, the uncertainties in electromagnetic force generation of a new class of manipulation systems are quantified. Subsequently, a drag-force uncertainty model for linear dynamics is proposed. This model can be employed for microrobots whose fluid dynamics are not well understood. A set of performance measures is introduced in the design of controllers, and a PID and a robust $\mathcal{H}_\infty$ controller are synthesized and evaluated through simulations. To demonstrate the capabilities of the synthesized controllers under localization and force uncertainties, low update rates are considered. The $\mathcal{H}_\infty$ controller can provably respect the performance measures under higher uncertainties than the PID controller, and its performance is further quantified through experiments in a prototype electromagnetic control system.**

***Note to Practitioners*—This paper is motivated by the problem of robust magnetic microrobot control for *in vivo* medical applications and micromanipulation. Existing approaches do not account for navigation system uncertainty, and rely on high imaging rates that are unrealistic for some applications (e.g., involving X-rays). We investigate the uncertainties in magnetic force generation and fluidic forces for microdevices that move in viscous fluid, considering state-of-the-art electromagnetic control systems capable of 5 degree-of-freedom control. These systems have not been examined before from this perspective. We demonstrate how to estimate the uncertainty in electromagnetic force generation due to localization and calibration inaccuracies, as well as the uncertainty in drag force due to microrobot shape complexity. Finally, we show that we can robustly control permanent magnetic microrobots in low viscosity oils, thus enabling more accurate and less restricted manipulation.**

***Index Terms*—Control, electromagnetism, microrobotics, robust, servoing, wireless.**

I. Introduction

MICROROBOTS are envisioned as a potential solution to challenging micromanipulation problems. Their ability to be dexterously controlled make them ideal tools for microassembly [2], protein-crystal handling [3], or cell manipulation [4]. Additionally, microrobots are an emerging tool for minimally invasive interventions, as their minuscule dimensions allow the navigation of natural pathways [5]. For example, microrobots have been proposed for kidney stone removal [6], intravascular drug delivery [7], intraocular drug delivery [8], and drug delivery in the brain [9].

Manuscript received September 10, 2012; revised April 02, 2013; accepted May 14, 2013. This paper was recommended for publication by Associate Editor C. Clevy and Editor D. Popa upon evaluation of the reviewers' comments. H. Marino and C. Bergeles contributed equally to this paper.*(Corresponding author: C. Bergeles.)* This paper was presented at the IEEE International Conference on Robotics and Automation, St. Paul, Minnesota, May 2012.

H. Marino is with Research Center "E. Piaggio," University of Pisa, Pisa 56127, Italy (e-mail: hamal.marino@gmail.com).

C. Bergeles is with the Hamlyn Centre, Imperial College London, London SW7 2AZ, U.K. (e-mail: christosbergeles@gmail.com).

B. J. Nelson is with the Institute of Robotics and Intelligent Systems, ETH Zurich, Zurich 8092, Switzerland (e-mail: bnelson@ethz.ch).

Digital Object Identifier 10.1109/TASE.2013.2265135

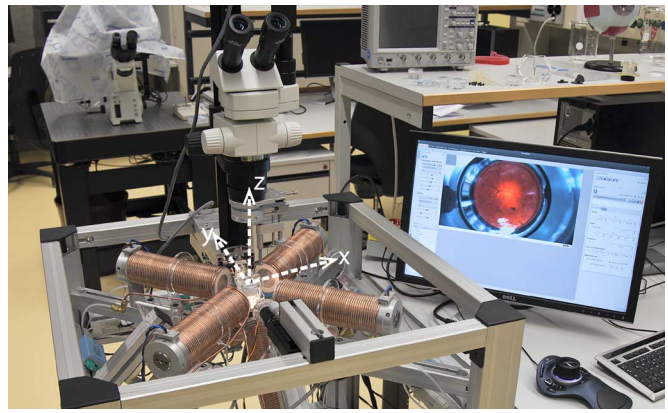

Fig. 1. The OctoMag electromagnetic control system for navigation of microrobots in the eye cavity. The microrobots will be inserted through a scleral incision, and will "swim" through vitreous humor or replacements to reach the retina [8].

A variety of methods, including electrostatic fields [10], thermal gradients [11], and bacterial propulsion [12], [13], have been proposed for microrobot actuation. The most common actuation methods, however, are based on electromagnetic fields, either by employing permanent magnets [14], magnetic resonance (MR) [7], or systems comprising arrays of electromagnets [2], [15] (see Fig. 1).

Accurate control of microrobots with electromagnetic fields requires precise localization information as dictated by "Earnshaw's theorem"; even in open-loop position control, magnetic controllers require knowledge of the position to apply the necessary fields and gradients [16].

Localization in the case of micromanipulation is achieved through direct visualization using optical microscopes [2], [3]. In *in vivo* applications, however, imaging and localization are complex tasks. While MRI systems allow the use of a single platform and pulse-sequence interleaving for both imaging/localization and actuation of magnetic microrobots, the stabilization of the feedback controller is challenging [7]. Custom-made electromagnetic control systems allow the generation of high gradients along relatively large distances but require coupling to an imaging system [16], [17].

Localization uncertainties result from poor algorithm performance or imaging resolution. Erroneous estimation of a microrobot's position leads to miscalculation of the required electromagnetic field and gradient and may lead to unstable control. Similarly, accurate knowledge of the steering system's parameters is not always a realistic assumption due to modeling errors and manufacturing inaccuracies. Therefore, controllers need to account for uncertainty in microdevice location, system parameters, and the environment.

Control of a magnetically levitated microrobot with 3 degrees of (translational) freedom (DOF) was examined in [18], where the authors also present considerations on the design of an electromagnetic control system. No uncertainties are taken into consideration in that work. Optimal magnetic control of a ferromagnetic particle is examined in [19] in 2D and 3D, however, only 2D experimental results are presented. The work presented in [20] proposes an adaptive backstepping controller and optimization methodology that estimates environmental parameters (such as the dielectric constant of the blood) for intravascular microrobot steering using MRI. Finally, uncertain location in control with rotating permanent magnets is studied in [14].

The current paper introduces methodologies for estimating the force uncertainties in magnetic microrobot steering, and for developing stable controllers for 5-DOF manipulation. The focus is on electromagnetic force uncertainty due to steering system complexity and low

localization rates, and drag force uncertainty due to microrobot shape complexity. We consider free floating microrobots that navigate in fluids that do not exhibit motion, e.g., the cerebrospinal fluid that fills the lateral brain ventricles, or the vitreous humor of the eye.

This paper is organized in sections based on the proposed system modeling and controller design workflow.

- Section II: Model the steering system and estimate uncertainties in force generation.
- Section III: Based on the microrobot's shape, numerically find its drag coefficients, linearize the dynamics, and account for the linearization inaccuracies.
- Section IV: Decide on a set of performance measures for controllers.
- Section V: Synthesize controllers (e.g., a PID and an $\mathcal{H}_\infty$ controller) and investigate their robustness with respect to uncertainties.
- Section VI: Experimentally evaluate the controller that respects the robustness and stability criteria.

This paper concludes in Section VII with a summary and discussion of the main contributions.

II. Actuation Principles and System Dynamics

A. Electromagnetic Manipulation

Recently, Kummer *et al.* presented five DOF micromanipulation of magnetic microrobots using arrays of electromagnets equipped with soft-magnetic cores [15]. The soft-magnetic cores enable the projection of fields across long distances and the generation of high field gradients. The electromagnets operate in the linear region of the near-ideal core material.

When current passes through each electromagnet, the generated field and gradient is affected by all the cores. This effect can be calibrated by measuring the field and gradient generated by each individual electromagnet *in situ*. The individual field contributions are then modeled as a point dipole [15]

$$\vec{B}(\vec{\Gamma},\vec{P}) = \frac{\mu_0}{4\pi\|\vec{P}\|^3}\left(\frac{3(\vec{\Gamma}\cdot\vec{P})\vec{P}}{\|\vec{P}\|^2} - \vec{\Gamma}\right) \tag{1}$$

where $\vec{\Gamma}$ [Am^2] is the point dipole, μ_0 $[(Tm)/(A)]$ is the vacuum permeability, and $\vec{P}$ [m] is the vector connecting the point where the field is calculated and the point dipole. Since the soft-magnetic cores operate in their linear region and a system with negligible hysteresis is assumed, the individual fields and gradients superimpose

$$\vec{B}(\vec{P}) = \sum_{e=1}^{n}\vec{B}_e(\vec{P}) = \sum_{e=1}^{n}\tilde{\vec{B}}_e(\vec{P})i_e = \mathcal{B}(\vec{P})I \tag{2}$$

$$\frac{\partial\vec{B}(\vec{P})}{\partial\square} = \sum_{e=1}^{n}\frac{\partial\vec{B}_e(\vec{P})}{\partial\square} = \sum_{e=1}^{n}\frac{\partial\tilde{\vec{B}}_e(\vec{P})}{\partial\square}i_e = \mathcal{B}_\square(\vec{P})I \tag{3}$$

where $e = 1,\cdots,n$ denotes the eth electromagnet, i_e is the current flowing through it, $\tilde{\vec{B}}_e$ is the unitary-current field, $\mathcal{B}(\vec{P}) = [\tilde{\vec{B}}_1(\vec{P})\cdots\tilde{\vec{B}}_n(\vec{P})]$ is a $3\times n$ field matrix, $I = [i_1\cdots i_n]^T$, and $\square \in \{x,y,z\}$ denotes the partial derivative of $\vec{B}$ in the respective direction.

The electromagnetic field is controlled to generate the desired torque and force on the magnetic microrobot. A microrobot moving in low viscosity fluid can align with the applied field unimpeded. Thus, it is possible to directly control the field orientation rather than the torque. The force on the microrobot is controlled through the field gradients

$$\vec{F} = \begin{bmatrix}\vec{B_x} & \vec{B_y} & \vec{B_z}\end{bmatrix}^T\vec{M} \tag{4}$$

where $\vec{M}$ is the microrobot's magnetic moment.

Combining (2)–(4) leads to

$$\begin{bmatrix}\vec{B}\\ \vec{F}\end{bmatrix} = \begin{bmatrix}\mathcal{B}(\vec{P})\\ \vec{M}^T\mathcal{B}_x(\vec{P})\\ \vec{M}^T\mathcal{B}_y(\vec{P})\\ \vec{M}^T\mathcal{B}_z(\vec{P})\end{bmatrix}\begin{bmatrix}i_1\\ \vdots\\ i_n\end{bmatrix} = \mathcal{A}_{B,F}(\vec{M},\vec{P})I \tag{5}$$

which describes the relationship between the field $\vec{B}$, the force $\vec{F}$, and the currents that flow through the electromagnets. The $6\times n$ matrix $\mathcal{A}_{B,F}$ is called the force-actuation matrix, and is a matrix characteristic of the system. It can be viewed as the "Jacobian" matrix of a traditional robotic mechanism. When the required field and force are known, the target currents can be calculated as

$$I = \mathcal{A}_{B,F}(\vec{M},\vec{P})^\dagger\begin{bmatrix}\vec{B}_{\mathrm{des}}\\ \vec{F}_{\mathrm{des}}\end{bmatrix} \tag{6}$$

where $\mathcal{A}_{B,F}(\vec{M},\vec{P})^\dagger$ is the pseudo-inverse of the force-actuation matrix.

B. Estimation of Uncertainties

The identification of the parameters involved in system modelling introduces errors. The range of uncertainty in the measurements, however, can be estimated based on the accuracy/relative tolerance of the measuring instrument, and the resulting force-generation errors can be accounted for in a calibration procedure.

The localization estimates that are supplied to the field controller can be noisy, both due to resolution limitations and algorithmic errors. Additionally, the discrete-time operation of imaging systems and the unobserved motion of the microrobot between two successive samples further contribute to localization uncertainty. While the algorithmic precision and accuracy can be calculated in controlled and simulated scenarios, their implications and the effect of position discrepancy between successive samplings on electromagnetic force generation has not been previously studied.

Electromagnetic control is a force-control approach, and to estimate the force uncertainty that is introduced due to the unobserved motion of the microrobot and localization inaccuracies, the force-actuation matrix of (5) can be used. Then, uncertainty in the microrobot's position can be related to uncertainty in the exerted electromagnetic force.

For a given permanent magnetic microrobot, the magnetic moment $\vec{M}$ has a fixed magnitude and is parallel to the electromagnetic field $\vec{B}$. Thus, we examine the matrix

$$\mathcal{A}_F(\vec{M},\vec{P}) = \begin{bmatrix}\vec{M}^TB_x(\vec{P})\\ \vec{M}^TB_y(\vec{P})\\ \vec{M}^TB_z(\vec{P})\end{bmatrix} = \mathcal{A}_F(I,\vec{P}) \tag{7}$$

where $\vec{B}$ has been dropped from (5), as its magnitude and orientation is directly related to the currents.

By studying the singular values of $\mathcal{A}_F(I,\vec{P})$ for a representative set of currents in $\mathcal{I}(I\in\mathcal{I})$ over a predefined dense point grid $\mathcal{P}$ ($\vec{P}\in\mathcal{P}$) that is based on a precalculated localization inaccuracy (refer to Section II-D), an estimate of the force uncertainty is obtained. In effect, we are seeking the ∞-norm of the set of relative changes in singular values

$$\mathcal{U} = \left\{\frac{\|\lambda_i\{\mathcal{A}_F(\vec{I},\vec{P}_j)\}-\lambda_i\{\mathcal{A}_F(\vec{I},\vec{P}_k)\}\|}{\|\lambda_i\{\mathcal{A}_F(\vec{I},\vec{P}_j)\}\|}\frac{1}{\|\vec{P}_j-\vec{P}_k\|}\right\} \tag{8}$$

where $\lambda_i(\mathcal{A}_F)$, $i\in\{1,2,3\}$ are the singular values of $\mathcal{A}_F$, $\vec{P}_j\in\mathcal{P}$ is the point in the discretized space that is under examination, and $\vec{P}_k\in\mathcal{N}(\vec{P}_j)$ are the direct horizontal, vertical, and diagonal neighbors of $\vec{P}_j$ in grid $\mathcal{P}$. For each set of currents I, the denominator in

(8) is the expected "force" amplification at point $\vec{P}_j$ (the actual microrobot position), while the numerator is the error in amplification if the microrobot is localized in $\vec{P}_k$. Their ratio, normalized by the distance between the two points, is the amplification error due to localization inaccuracies. The ∞-norm of $\mathcal{U}$ is used as the uncertainty in force across the entire workspace.

C. Electromagnetic Steering System Dynamics

Robust controller design requires the identification and modeling of the dynamic components in the electromagnetic system. An electromagnetic array will experience non-negligible transitional phase due to the inductance of each coil. This can be modeled as a low-pass filter

$$\frac{1}{1+\tau_{\mathrm{ind}}\, s} = \frac{1}{1+\frac{L}{R}s} \tag{9}$$

where τ_{ind} [s] is the time constant, L [H] is the self-inductance, and R [Ω] the resistance of the coil.

The sampling rates need to be considered when operating at low frame rates. Time delays can be accounted for by using half of the sampling period as a time delay [21]

$$e^{-\tau_{\mathrm{fps}} s} = e^{-\frac{T_{\mathrm{fps}}}{2} s} \tag{10}$$

where T_{fps} is the image acquisition rate. Complex image processing for localization could introduce further delays that would be accounted for as an additional delay block. Most localization algorithms for robotics, however, are developed to operate in real-time, and, hence, little effect in the system's behavior is expected.

The controller inputs (e.g., the monitoring and setting of currents, the transmission of the position) are transmitted and processed with delays lower than 1 ms. Such delays would insert a phase distortion of 0.06 rad (3.4°) around the operational frequency of 10 Hz, which is the frequency of interest in this work. This phase distortion is very low and can be neglected.

The time delays can be approximated by first-order Padé functions [22], i.e., ratios of first-order polynomials

$$e^{-\tau s} \simeq \frac{1-\frac{\tau}{2}s}{1+\frac{\tau}{2}s}. \tag{11}$$

Padé approximants have unit magnitude and are phase shifted. They allow the consideration of the continuous equivalent of a discrete system and the synthesis of a continuous controller that is subsequently discretized.

D. Experimental Force Uncertainties and Dynamics

The OctoMag (see Fig. 1 for setup and coordinate frame), an array of eight electromagnets arranged in a hemispherical configuration, is designed for intraocular interventions with microrobots. The current version can accommodate a small animal. The soft-magnetic cores of the electromagnets are of a CoFe alloy, which can be considered a near-ideal material. Thus, the electromagnetic fields and gradients generated by each electromagnet superimpose. The OctoMag allows the generation of 30 mT field, with a gradient of 1.5 T/m at the center of the workspace. The manipulation workspace is $10 \times 10 \times 10$ mm^3, which covers the posterior eye segment.

The OctoMag's dynamic parameter values were obtained from [15]. Our goal is to steer microrobots with a low image acquisition rate. Thus, a sampling rate of 7.5 Hz was chosen, which is lower than the data acquisition rate during fluoroscopy-based surgeries (20–30 fps) and the frame rate in MRI guidance of microrobots (24 fps in [7], continuous knowledge of position in [20]). The time constant due to inductance and the time delay due to the sampling rate are calculated as

$$\tau_{\mathrm{ind}} = \frac{L}{R} = \frac{94\times10^{-3}}{1.3} = 72.3\times10^{-3}\ \mathrm{sec} \tag{12}$$

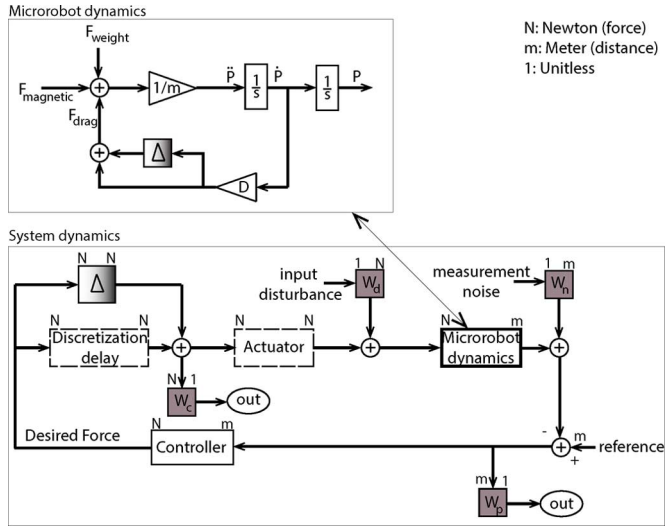

Fig. 2. Scheme for the uncertain linear system used for controller synthesis and analysis. $\mathrm{W_d}$ shapes the input disturbance, $\mathrm{W_n}$ the measurement noise, and $\mathrm{W_c}$ and $\mathrm{W_p}$ the performance requirements on control effort, and output error, respectively. The gradient-colored box denotes calculated uncertainty. The "actuator" block encapsulates the inductance filtering.

$$\tau_{\mathrm{fps}} = \frac{1}{2\times \mathrm{fps}} = \frac{1}{2\times 7.5} = 0.0667\ \mathrm{sec}. \tag{13}$$

To evaluate the uncertainties in force generation, we assume a tracking imprecision on the order of 0.5 mm, as calculated in [16] for intraocular applications. Additionally, [15] and [16] report a worst-case microrobot drift on the order of 0.5 mm/s in the absence of accurate localization. During our experimental work, we achieved several millimeters per second velocities.

Assuming a microrobot speed on the order of 4 mm/s, and including the tracking inaccuracies and potential drift, the position discrepancy between each sampling cycle (1/7.5 s) will be on the order of 1 mm. Thus, the normalizing factor of distance between points of the grid $\mathcal{P}$ used in (8) is chosen to be 1 mm, which leads to a force uncertainty

$$\|\mathcal{U}\|_\infty = \delta_{\mathrm{norm}} = 0.5\ (50\%) \tag{14}$$

this means that, for a 1 mm error in position, the worst-case force uncertainty across the entire workspace is 0.5.

The layout for the uncertain linear model corresponding to the electromagnetic control system is depicted in Fig. 2. The block Δ represents a full 3×3 block of uncertainties with ∞-norm bounded by δ_{norm}, which is calculated in (14). In Fig. 2, "reference" denotes the desired position of the microrobot.

III. Orientation-Dependent Microrobot Dynamics

In MRI actuated systems the electromagnetic field cannot be used to reorient magnetic microrobots, and, as a result, spherical magnetic devices are usually considered [7], [20]. Their drag forces are unaffected by orientation. To manipulate arbitrarily shaped microrobots, however, the orientation-dependent microrobot dynamics need to be examined

$$\vec{F}_{\mathrm{mag}} + \vec{F}_{\mathrm{drag}} + \vec{F}_{\mathrm{weight}} = m\vec{a} = m\ddot{\vec{P}} \tag{15}$$

where $\vec{F}_{\mathrm{mag}}$ [N] is the magnetic force, $\vec{F}_{\mathrm{drag}}$ [N] is the drag force, $\vec{F}_{\mathrm{weight}}$ [N] is the force due to the apparent weight of the microrobot (*i.e.*, includes gravity force and buoyancy force), and m [kg] and $\vec{a}$ [m/s^2] are the mass and the acceleration of the microrobot, respectively, and $\vec{P}$ [m] is its position.

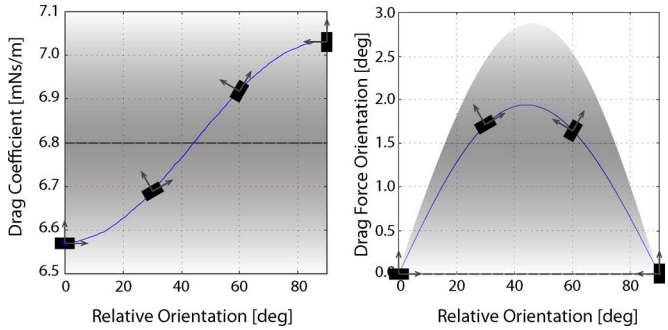

Fig. 3. Actual drag on a cylindrical microrobot of 1 mm length and 0.5 mm base diameter. The drag coefficient and orientation are shown with respect to relative orientation of the microrobot, which is depicted as a rectangle. The overlaid gradient shows the uncertainty margins in the drag coefficient and drag force orientation. Figures are for a microrobot moving along the x axis.

We are operating at low-Reynolds regimes (on the order of $\mathrm{Re} = 10^{-3} - 10^{-2}$) and, thus, the drag is linear

$$\vec{F}_{\mathrm{drag}} = -D^{\mathrm{w}}\vec{v} \tag{16}$$

where D^{w} is a matrix of drag coefficients and $\vec{v}$ is the relative velocity between the body and the fluid. D^{w} depends on the geometrical properties of the body and the coordinate frame in which the drag force is computed (w denotes the world coordinate frame).

The intrinsic matrix D^{b}, on the other hand, depends only on the properties of the microrobot. The matrix can be computationally estimated using a CAD model of the device, knowledge of the fluid's parameters, and the method of regularized Stocklets [23]. Then, for different microrobot orientations

$$\vec{F}_{\mathrm{drag}} = -D^{\mathrm{w}}\vec{v} = -R^{\mathrm{w}}_{\mathrm{b}} D^{\mathrm{b}} R^{\mathrm{w}\,T}_{\mathrm{b}} \vec{v} = -R^{\mathrm{w}}_{\mathrm{b}} D^{\mathrm{b}}_0 R^{\mathrm{w}\,T}_{\mathrm{b}} \mu_f \vec{v} \tag{17}$$

where $R^{\mathrm{w}}_{\mathrm{b}}$ denotes body-frame to world-frame rotation, D^{b}_0 is the intrinsic matrix for unit viscosity and μ_f [m^2/s] the viscosity of the fluid. The numerical calculation of the drag-force coefficients for complex microrobot shapes is an open research problem, and, in the general case, leads to nonlinear orientation/configuration dependent fluid dynamic equations even at low Reynolds numbers. The methodology we subsequently introduce uses a numerically estimated D^{b} matrix and force uncertainties to create a linear dynamics system that additionally accounts for numerical estimation errors.

A. Estimation of Uncertainties

We will examine a 1 mm long, 0.5 mm diameter cylindrical NdFeB permanent magnetic microrobot. Its drag-matrix D^{b}_0 was estimated using the CAD-based method [23]

$$D^{\mathrm{b}}_0 = \begin{bmatrix} 6.57 & 0 & 0 \\ 0 & 7.03 & 0 \\ 0 & 0 & 7.03 \end{bmatrix} \times 10^{-3}. \tag{18}$$

The matrix D^{b}_0 has the drag coefficients of each principal direction of the cylinder. Contrary to a spherical microrobot, which would have identical coefficients along the diagonal, the drag-force acting on the cylinder is not necessarily parallel to its velocity. Fig. 3 shows the drag coefficient and drag-force orientation for different orientations of the microrobot.

With the goal of having a linear uncertain system for the microrobot dynamics, we use a sphere model for the drag force and account for the inconsistency between the actual drag and the simplification through an uncertainty margin. Since many microrobots of interest have complex shapes, the uncertainty margin can be made large enough to cover uncertainty in the drag coefficients.

TABLE I
DATA OF THE CYLINDRICAL NDFEB MICROROBOT

Volume	Density	Weight	Magnetic moment
0.196 mm^3	7450 kg/m^3	14.4 μN	0.00027 Am^2

Fig. 3 and matrix D^{b}_0 show that the drag coefficient for the cylindrical microrobot ranges from 6.57×10^{-3} Ns/m to 7.03×10^{-3} Ns/m. An "equivalent" sphere has a diameter

$$d = \frac{6.57 \times 10^{-3} + 7.03 \times 10^{-3}}{2 \times 3\pi} = \frac{6.8}{3\pi} \times 10^{-3}\,\mathrm{m} \tag{19}$$

which is found by averaging the extreme coefficients of D^{b}_0. To cover the range of the cylinder's drag coefficient, i.e., the discrepancy between the calculated coefficient and the maximum value of D^{b}_0, a relative uncertainty term is inserted

$$\delta_{\mathrm{drag}} \geq \frac{(7.03 - 6.8) \times 10^{-3}}{6.8 \times 10^{-3}} \simeq 0.034. \tag{20}$$

A higher value of $\delta_{\mathrm{drag}} = 0.05$ (5%) was chosen to account for drag-coefficient misestimation due to numerical errors. Superimposing this relative uncertainty on the drag coefficient of the "equivalent" sphere covers all possible drag coefficients and orientations of the cylindrical microrobot. The orientation uncertainty covers angles on a sphere around the direction of the motion of the microrobot (Fig. 3).

For the spherical microrobot of diameter d moving in a fluid with viscosity μ_{f} at a velocity $\vec{v}$, $F_{\mathrm{drag}} = 3\pi\mu_{\mathrm{f}} d\vec{v}$. The state-space model is

$$\dot{\vec{x}} = \begin{bmatrix} 0_3 & I_3 \\ 0_3 & -\frac{1}{m} 3\pi\mu_{\mathrm{f}} d I_3 \end{bmatrix} \vec{x} + \begin{bmatrix} 0_3 \\ \frac{1}{m} I_3 \end{bmatrix} (F_{\mathrm{mag}} + F_{\mathrm{weight}}) \tag{21}$$

where $\vec{x} = [\vec{P}^T, \dot{\vec{P}}^T]^T$ is the state vector. The schematic of the dynamics is shown in Fig. 2, where Δ represents uncertainties for which $\|\Delta\|_\infty = \delta_{\mathrm{drag}}$, triangular blocks signify multiplications, $D = 3\pi d I_3 \mu_f$ is the drag coefficient matrix, and m is the microrobot mass which is considered uncertain within $\pm 10\%$ of its nominal 1.46×10^{-6} kg value. The high uncertainty in the mass stems from inaccuracy in the measurement of the weight of the microrobot. All microrobot data are given in Table I. The magnetic moment was estimated based on the magnetization measured in [20] for a NdFeB sphere of the same manufacturer.

IV. PERFORMANCE MEASURES

The complete system, including the delay blocks, the microrobot dynamics block and the uncertainties, is shown in Fig. 2. Letters above each block denote the input and output units, with 1 signifying a normalized value. Each grayed block signifies a shaping function. More specifically, these blocks cover four discrete aspects of the system: 1) final controller (position) error; 2) control weight; 3) model noise; and 4) measurement noise. They can be classified as performance measures for the controller that must be satisfied despite the uncertainties, and disturbances.

These blocks/functions "shape" the frequency behavior of their input variable and perform magnitude normalization. Here, the normalization value was chosen to be 10^{-3}, in order to represent [mm] in distance, [mN] in force, etc.

A. Performance Measures

As a first step to controller synthesis, we established performance measures that need to be respected by the controllers within the uncertainty margins. Blocks W_c and W_p in Fig. 2 represent these performance measures.

Block W_c represents the weight on control effort. Based on [15], the maximum force that the system can apply on the microrobot under different configurations is on the order of 100 μN. $W_c = 10$ leads to the desired normalization order, while limiting the control effort

$$W_c = 10. \tag{22}$$

Block W_p is the weight on final position error. The requirement is to have a maximum steady-state error of 100 μm. Thus, the static gain of W_p is 10. The cutoff frequency is chosen to be 0.1 rad/s, leading to a small bandwidth. This is necessary for obtaining an achievable set of requirements

$$W_p = 10\frac{1+10^{-1}s}{1+10s}. \tag{23}$$

B. Disturbances Model

The known characteristics of the input disturbances are represented by block $\mathrm{W_d}$ in Fig. 2. Such disturbances include uncertainty in weight or fluid viscosity.

In Fig. 2, block $\mathrm{W_d}$ represents known characteristics of the input disturbances, e.g., uncertainty in weight or fluid viscosity. These were selected to be in the range of [μN], since this is the order of magnitude of the forces acting on the microrobot. $\mathrm{W_d}$ has a static gain of 0.01 ($0.01 \times 1\ \mathrm{mN} = 10\ \mu$N) as the weight of an unknown force. The shaping function was implemented as a low-pass filter with a cutoff frequency of 10^2 rad/sec

$$W_d = 0.01\frac{1+10^{-4}s}{1+10^{-2}s}. \tag{24}$$

Block W_n is the weight for noise on output measurements. It represents localization errors due to tracking and infrastructure. Based on existing tracking algorithms developed for intraocular localization [16], the error has a mean value $\mu = 300\ \mu$m and a standard deviation $\sigma = 200\ \mu$m. W_n is implemented as a high-pass function with a cutoff frequency at 10^2 rad/sec and a high-frequency gain of 0.3, which accounts for uncertainties on the order of 300 μm

$$W_n = 0.3\frac{1+s}{10^2+s}. \tag{25}$$

V. Controllers

A simple PID and an $\mathcal{H}_\infty$ controller were synthesized and evaluated using Matlab and Simulink.

A. PID Controller

1) Synthesis: Using a SISO version of the system without uncertainties (nominal system), *i.e.*, a serial connection of: (a) a delay due to discretization (11); (b) a low-pass filter due to the actuation (9); and (c) a single-dimensional version of (21), a PID controller was synthesized. On the nominal SISO system, a 60° phase margin and 3 rad/s bandwidth were achieved.

2) Analysis and Simulation: Fig. 4 shows the simulated three-dimensional step response for a MIMO version of the PID controller. The MIMO version consists of a diagonal 3×3 controller, where each nonzero entry corresponds to the SISO controller synthesized previously. The response characteristics of the SISO and MIMO systems are shown in Table II.

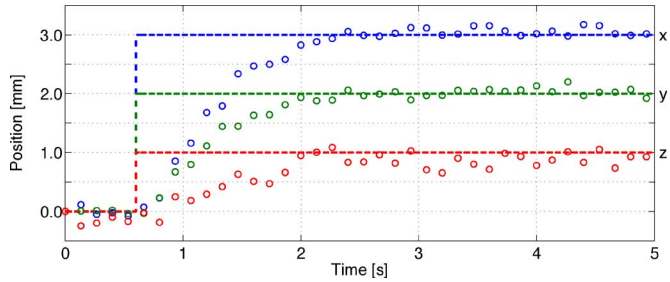

Fig. 4. Step response for the synthesized PID controller at 7.5 Hz image rate. The dashed line corresponds to the reference input, and the ∘ to the sampled measurements. Since the orientation of the microrobot negligibly affects the simulation results, we only show the results for the x-orientation.

TABLE II
PID Controller Performance

Metric	Nominal	Simulation		
		x	y	z
95% Rise time [s]	0.58	2.05	2.09	3.6
Overshoot [%]	7.2	2	1.5	0
10% Settling time [s]	0.54	1.81	1.84	3.27

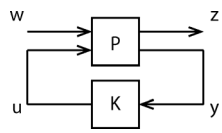

Fig. 5. Scheme of the high-level system interconnection, which can be represented in Linear Fractional Transformation form: w and u are exogenous and controllable inputs, and z and y are controlled and measured outputs of the plant P; K is the controller.

Using robustness analysis (μ-analysis tool in Matlab), however, the system was shown to be robustly stable up to $\delta_{\mathrm{norm}} = 0.25$. This margin is less than what is required by the localization and force uncertainties (see Section II-B), and, for this reason, robust $\mathcal{H}_\infty$ control was explored.

B. $\mathcal{H}_\infty$ Controller

1) Synthesis: $\mathcal{H}_\infty$ control is used to suppress the effect of uncertainties by minimizing the ∞-norm of the system's closed-loop transfer function. To avoid the theoretical and numerical complexity of the optimal solution to the stated minimization problem, the suboptimal $\mathcal{H}_\infty$ problem is solved

$$\text{Given } \gamma > 0 \text{ find all controllers : } \|\mathcal{F}_{zw}(P,K)\|_\infty < \gamma \tag{26}$$

where P is the plant, K is the controller, and $\mathcal{F}_{zw}(P,K)$ is the system's transfer function represented in Linear Fractional Transformation (LFT) form [24]. We use w to represent exogenous inputs that cannot be controlled, e.g., measurement noise and disturbances; u to represent controllable inputs; z to indicate controlled inputs that need to be minimized and variables used to set performance objectives. Finally, y represents the measured outputs. A visual representation of the high-level interconnection can be seen in Fig. 5. The LFT is the transfer function between w and z, considering a closed-loop around K, which has inputs y and outputs u.

For a system that contains uncertainties and can be represented in LFT with a matrix Δ, the Robust Stability Theorem states that a sufficient condition for stability in a "robust to uncertainty" sense is

$$\|\Delta\|_\infty \leq \frac{1}{\gamma}. \tag{27}$$

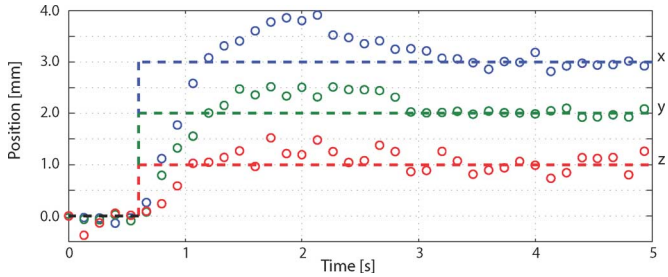

Fig. 6. Step response for the synthesized $\mathcal{H}_\infty$ controller. The dashed line corresponds to the reference input, and the ∘ to the sampled measurements. The orientation of the microrobot negligibly affects the simulation results, and, hence, we only show the results for the x-orientation.

TABLE III
$\mathcal{H}_\infty$ CONTROLLER PERFORMANCE IN SIMULATIONS

	Simulation		
Metric	x	y	z
95% Rise time [s]	0.57	0.65	0.53
Overshoot [%]	26.8	24.5	30.6
10% Settling time [s]	2.77	2.77	2.77

In this paper, an $\mathcal{H}_\infty$ controller is synthesized using the *DK*-iteration method. A controller K is obtained for the maximum δ_{norm} such that

$$\sup_{\omega\in\mathbb{R}} \mu_{\underline{\Delta}}(\mathcal{F}(P,K)) \leq \frac{1}{\delta_{\text{norm}}} = \frac{1}{\|\Delta\|_\infty} \tag{28}$$

where ω represents the frequency, μ is the structured singular value of $\mathcal{F}(P,K)$, and $\underline{\Delta}$ is the set of the possible perturbations in the system. The controller was synthesized using the robust control DK-iteration tools.

2) Analysis and Simulation: The controller was analyzed with μ-analysis tools. A model-order reduction was performed [24], keeping only the states with Hankel singular values greater than $1/1000$ of the maximum value. The reduced controller was found robustly stable and exhibited robust performance for $\delta_{\text{norm}} = 0.5$, which was a margin calculated in Section II-B. This value corresponds to one-body-length localization uncertainty between two successive image acquisitions.

The response of the system with the implemented control law for step inputs in three dimensions is shown in Fig. 6. The characteristics of the response are summarized in Table III.

VI. EXPERIMENTS

Experiments were performed in the OctoMag using a controller implemented in C++. The image acquisition rate was 7.5 Hz. Due to the asynchronous communication of our software system, the controller was selected to operate at 15 Hz to satisfy the Nyquist criterion. The permanent magnetic microrobot moved in a 350 mm^2/s viscosity oil with density of 0.97 g/cm^3 [Wacker® AK350], similar to oils which vitreoretinal surgeons may use as a vitreous humor replacements. The microrobot's position was estimated using a pair of calibrated orthogonal microscopes. The device was tracked using background subtraction and morphological filtering, and, then, its 3D position in the workspace was estimated via triangulation. Noise was added to match the values used in the simulations. A position was considered to be "reached" when the microrobot was within 100 μm from it, as was implemented in the requirements.

The step response for two different orientations was performed. The microrobot was commanded to reach point $(-3.0, -2.0, -1.0)$ mm [Fig. 7(a) and (b)]. It can be seen that the controller succeeded in steering the microrobot according to the specified requirements

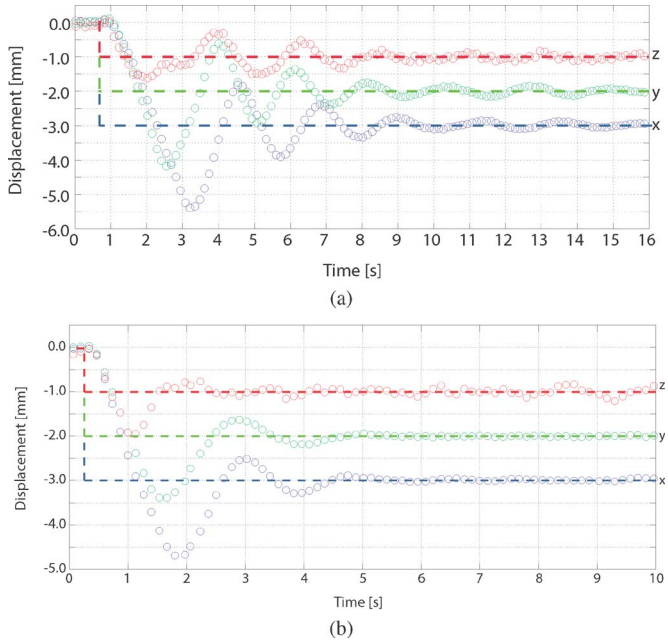

Fig. 7. Experimental results for the NdFeB microrobot moving in 350 mm^2/s viscosity oil. (a) Step response for a microdevice aligned along the x axis. (b) Step response for a microdevice aligned along the z axis.

TABLE IV
$\mathcal{H}_\infty$ CONTROLLER PERFORMANCE IN STEP EXPERIMENTS

	Step experiment					
	x align			z align		
Metric	x	y	z	x	y	z
95% Rise time [s]	1.6	1.09	0.71	0.93	0.8	0.5
Overshoot [%]	79.8	108.5	62	56.2	65	95.2
10% Settling time [s]	6.55	7.64	8.3	3.22	3.09	2.17

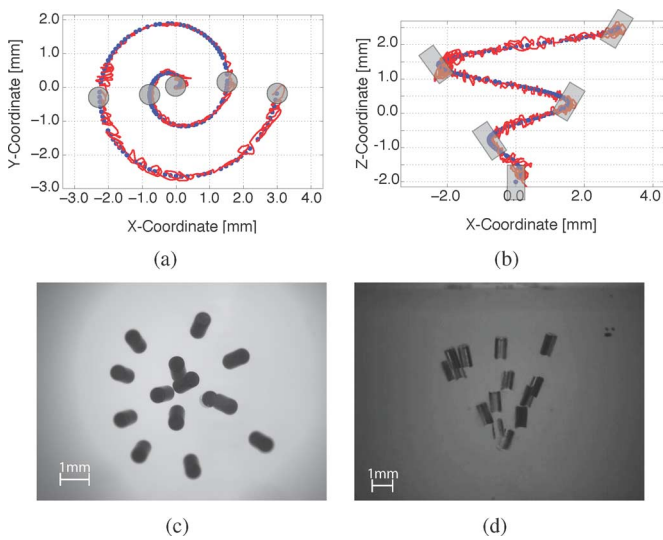

Fig. 8. Microrobot moving along a spiral trajectory, while oriented to the start of the trajectory. (a) and (c) Top view. (b) and (d) Side view. Images (c) and (d) are composite images depicting a single microrobot at different time frames.

accounting for unobserved motion due to the low frame rates, localization uncertainties due to tracking, and uncertainties due to modeling inaccuracies. The overshoot, rise time and settling time values can be found in Table IV, and, as can be seen, they are in overall agreement with the simulations.

To investigate the controller's behavior in a more complex navigation example, the microrobot was commanded to move along a spiral trajectory while orientated towards a fixed point. This trajectory and the corresponding microrobot path can be seen in Fig. 8. As before, noise was added to the localization algorithm. The errors between the trajectory and the microrobot's path can be measured from the plotted figures using functionality provided by Matlab. The maximum error along the x-coordinate is approximately 320 μm, along the y-coordinate 270 μm, and along the z-coordinate 490 μm. These errors are on the order of the errors introduced in localization. This is the first controller to navigate permanent magnetic microrobots in low viscosity oil and low frame rate using an electromagnetic system with ferrous cores.

VII. Conclusion and Discussion

In this paper, we discussed a methodology to account for uncertainty in the force generated by a new class of electromagnetic control systems that allow the generation of high electromagnetic field gradients to guide magnetic microrobots. Additionally, we introduced a method to incorporate uncertain but linear fluid dynamics for complex microrobot shapes. We synthesized two types of controllers, a traditional PID controller and an $\mathcal{H}_\infty$ controller, and compared their behavior with respect to uncertainties and established performance measures. Subsequently, we introduced additional realistic system disturbances and demonstrated the robust behavior of the $\mathcal{H}_\infty$ controller both in simulations and experiments. The image sampling rate was one of the lowest reported in electromagnetic microrobot control, and it was shown that with robust controller synthesis *in vivo* microrobot navigation with techniques such as fluoroscopy can be considered while avoiding damaging radiation doses to the patient.

The methods introduced in this paper constitute one of the first efforts to estimate force uncertainties in a complex electromagnetic control system. The simplification of the microrobot dynamics is generalizable and can be used for microrobots whose fluid dynamics are not well understood.

This framework can be further augmented depending on the application. Even though only free floating microdevices were considered, adhesion forces between the microrobot and the physiological surface may be present. Additionally, if fluidic motion is present, the drag force must be updated. In smaller scales, electrostatic forces and van der Waals forces may need consideration [20]. These forces can be incorporated in the mathematical formulation and can be linearized and tied to estimated uncertainties following the proposed drag force approach.

This paper considered microrobots in low Reynolds regimes, which allowed for a simplification of the fluidic drag forces. To apply the mathematical methodology for larger magnetically guided devices, such as capsule endoscopes, more complex nonlinear modelling that is outside the scope of this paper is required. The electromagnetic force uncertainty estimation, however, would be directly applicable.

To navigate microrobots in fluids of lower viscosity, for example, cerebrospinal fluid, it is important to understand the trade-offs between sampling rate and viscosity. A higher viscosity relaxes the necessity for high frame rates, which are needed to account for unobserved microrobot motions in fluids with low damping. Thus, the proposed methodologies for uncertainty estimation can still be applied, but the sampling rates must be adjusted according to the application.

Finally, even though MRI-based control shares similar principles with the investigated control methodologies, direct translation of the proposed method to that domain is not possible. Such translation would require accounting for the slew rate of the MRI system and the effect that imaging sequences have on the actuating microrobots. The proposed drag force uncertainty estimation, however, is directly applicable.

References

[1] H. Marino, C. Bergeles, and B. J. Nelson, "Robust H-∞ control for electromagnetic steering of microrobots," in *Proc. IEEE Int. Conf. Robot. Autom.*, 2012, pp. 2498–2503.

[2] E. Diller, C. Pawashe, S. Floyd, and M. Sitti, "Assembly and disassembly of magnetic mobile micro-robots towards deterministic 2-D reconfigurable micro-systems," *Int. J. Robot. Res.*, vol. 30, no. 14, pp. 1667–1680, 2011.

[3] H. Tung, D. R. Frutiger, S. Pané, and B. J. Nelson, "Polymer-based wireless resonant magnetic microrobots," in *Proc. IEEE Int. Conf. Robot. Autom.*, 2012, pp. 715–720.

[4] M. S. Sakar, E. B. Steager, M. J. Kim, G. J. Pappas, and V. Kumar, "Single-cell manipulation using ferromagnetic composite microtransporters," *Appl. Phys. Letts.*, vol. 96, no. 043705, pp. 1–3, 2010.

[5] B. J. Nelson, I. K. Kaliakatsos, and J. J. Abbott, "Microrobots for minimally invasive medicine," *Annu. Rev. Biomed. Eng.*, vol. 12, pp. 55–85, 2010.

[6] J. Edd, S. Payen, B. Rubinsky, M. L. Stoller, and M. Sitti, "Biomimetic propulsion for a swimming surgical microrobot," in *Proc. IEEE/RSJ Int. Conf. Intell. Robot. Syst.*, 2003, pp. 2583–2588.

[7] S. Martel, O. Felfoul, J. Mathieu, A. Chanu, S. Tamaz, M. Mohammadi, M. Mankiewicz, and N. Tabatabaei, "MRI-based medical nanorobotic platform for the control of magnetic nanoparticles and flagellated bacteria for target interventions in human capillaries," *Int. J. Robot. Res.*, vol. 28, no. 9, pp. 1169–1182, 2009.

[8] C. Bergeles, M. P. Kummer, B. E. Kratochvil, C. Framme, and B. J. Nelson, "Steerable intravitreal inserts for drug delivery: *In vitro* and *ex vivo* mobility experiments," in *Proc. Int. Conf. Med. Image Comput. Comput. Assisted Intervention*, 2011, pp. 33–40.

[9] S. N. Tabatabaei, S. Duchemin, H. Girouard, and S. Martel, "Towards MR-navigable nanorobotic carriers for drug delivery into the brain," in *Proc. IEEE Int. Conf. Robot. Autom.*, 2012, pp. 727–732.

[10] B. R. Donald, C. G. Levey, C. D. McGray, I. Paprotny, and D. Rus, "An untethered, electrostatic, globally controllable MEMS micro-robot," *IEEE J. Microelectromech. Syst.*, vol. 15, no. 1, pp. 1–15, 2006.

[11] W. Hu, K. S. Ishii, and A. Ohta, "Micro-assembly using optically controlled bubble microrobots in saline solution," in *Proc. IEEE Int. Conf. Robot. Autom.*, 2012, pp. 733–738.

[12] M. S. Sakar, E. B. Steager, D. H. Kim, K. Agung, M. Kim, V. Kumar, and G. Pappas, "Modeling, control and experimental characterization of microbiorobots," *Int. J. Robot. Res.*, vol. 30, no. 6, pp. 647–658, 2011.

[13] V. Arabagi, B. Behkam, E. Cheung, and M. Sitti, "Modeling of stochastic motion of bacteria propelled spherical microbeads," *J. Appl. Phys.*, vol. 109, no. 114702, pp. 1–10, 2011.

[14] A. W. Mahoney and J. J. Abbott, "Control of untethered magnetically actuated tools with localization unvertainty using a rotating permanent magnet," in *Proc. IEEE Int. Conf. Biomed. Robot. Biomechatronics*, 2012, pp. 3375–3380.

[15] M. P. Kummer, J. J. Abbott, B. E. Kratochvil, R. Borer, A. Sengul, and B. J. Nelson, "OctoMag: An electromagnetic system for 5-DOF wireless micromanipulation," *IEEE Trans. Robot.*, vol. 26, no. 6, pp. 1006–1017, Dec. 2010.

[16] C. Bergeles, B. E. Kratochvil, and B. J. Nelson, "Visually servoing magnetic intraocular microdevices," *IEEE Trans. Robot.*, vol. 28, no. 4, pp. 798–809, Aug. 2012.

[17] K. Cha, S. Jeong, L. Qin, J. Park, and S. Park, "Electromagnetic actuation methods for intravascular locomotive microrobot," in *Proc. IEEE Int. Conf. Eng. Med. Biol.*, 2010, pp. 1962–1965.

[18] T. Nakamura and M. B. Khamesee, "A prototype mechanism for three-dimensional levitated movement of a small magnet," *IEEE/ASME Trans. Mechatronics*, vol. 2, no. 1, pp. 41–50, Mar. 1997.

[19] A. Komaee and B. Shapiro, "Steering a ferromagnetic particle by optimal magnetic feedback control," *IEEE Trans. Control Syst. Technol.*, vol. 20, no. 4, pp. 1011–1024, July 2012.

[20] L. Arcese, M. Fruchard, and A. Ferreira, "Endovascular magnetically-guided robots: Navigation modeling and optimization," *IEEE Trans. Biomed. Eng.*, vol. 59, no. 4, pp. 977–987, Apr. 2012.

[21] C. Bonivento, C. Melchiorri, and R. Zanasi, "Sistemi di controllo digitale," Progetto Leonardo. Bologna, Italy, 1995.

[22] W. S. Levine*, The Control Handbook*. Boca Raton, FL, USA: CRC, 1996.

[23] R. Cortez, L. Fauci, and A. Medivikov, "The method of regularized stokeslets in three dimensions: Analysis, validation, and application to helical swimming," *Phys. Fluids*, vol. 17, 2004.

[24] U. Mackenroth*, Robust Control Systems—Theory and Case Studies*. New York, NY, USA: Springer, 2003.